Eidgenössische Technische Hochschule Zürich
Swiss Federal Institute of Technology Zurich

Power Systems Laboratory

Johanna Vorwerk

Small-Signal Analysis of Power Systems with Low Rotational Inertia

Semester Thesis
PSL 1714

EEH – Power Systems Laboratory
Swiss Federal Institute of Technology (ETH) Zurich

Expert: Prof. Dr. Gabriela Hug
Supervisors: M.Sc. Uros Markovic

Zürich, February 5, 2026

Abstract

Due to the increasing share of renewable energy generation units, the physical inertia is decreasing in not only distribution but also transmission grids, leading towards low-inertia systems. However, the existing control schemes for Voltage Source Converters (VSCs), the power electronic grid interface used for renewable generation, mostly focus on microgrids that have different requirements than transmission grids. In this context a model for transmission grids is proposed.

We first present the VSC model used in this work and analytically describe each control block. The proposed model includes options to operate grid-forming and grid-feeding controllers and incorporates two different active power control schemes: active power droop control and virtual inertia emulation. After linearizing the model in order to apply standard control analysis, its implementation in MATLAB and verification is discussed. Having established the foundation, small-signal stability analyses are performed, showing that the converter configuration significantly affects stability margins. Besides optimizing the outer control loop parameters, the effect of the grid equivalent on overall system stability and the impact of the synchronization unit for grid-following converters are investigated. Simulations show that in general grid-forming converters provide larger stability margins. Indeed, grid-feeding converters operating with active power droop may not retain stability when connected to weaker grids.

Contents

List of Acronyms

AC	Alternating Current
APC	Active Power Control
DAE	Differential Algebraic Equation
DC	Direct Current
g-feed	Grid-Feeding Converter
g-form	Grid-Forming Converter
LHP	Left Half-Plane
LPF	Low-Pass Filter
PLL	Phase-Locked Loop
RPC	Reactive Power Controller
SM	Synchronous Machine
SCR	Short Circuit Ratio
SRF	Synchronous Reference Frame
SSM	Small-Signal Model
VIE	Virtual Inertia Emulation
VSC	Voltage Source Converter

List of Figures

List of Tables

Chapter 1

Introduction

The increasing share of renewable generation units connected to the transmission grid simultaneously extends the penetration of Voltage Source Converters (VSCs), that act as grid-interface. Due to their power electronic nature, the physical inertia of the generators is progressively decoupled from the network, resulting in low inertia systems and imposing new challenges regarding system stability [1]. In order to capture the system dynamics in the presence of these converters, new Differential-Algebraic Equation (DAE) models must be developed for the purpose of small-signal analysis.

The work in [2] investigated the stability of a VSC control scheme based on the virtual swing equation. However, there was no external power control included in the model, and the implementation of the damping restricted the applicability of the studied control system. An extension of this control design was presented in [3], where a frequency droop was included in the outer loop, together with the Phase Locked Loop (PLL) and virtual impedance. The same control system and the corresponding small-signal model was further elaborated and analyzed in [4]. Nonetheless, both approaches focus on a single power control design and put emphasis on the grid-connected operation only. Since the potential VSC control configurations [5–7], as well as the operation modes [8, 9] can be quite versatile, requirements for a more general modeling approach are emerging.

The contribution of this work is two-fold. First, we introduce a uniform VSC model with a detailed, state-of-the-art control structure. Two active power control approaches are proposed under different converter operation modes. Subsequently, a formulation of the DAE system, together with the respective small-signal model is derived. Second, the stability margins of different VSC configurations are investigated through eigenvalue analysis and various bifurcation studies.

The remainder of the report is structured as follows. In Chapter 2, a detailed VSC control scheme is presented, as well as the respective mathematical formulation of the problem and the resulting DAEs. Furthermore, it describes the small-signal modelling

and derives the state-space representation. Chapter 3 outlines the implementation of the non-linear and small-signal models in MATLAB, respectively. Moreover, it includes the operation parameters and presents simulation results for the validation of the presented models. Chapter 4 showcases the stability analyses results, whereas chapter 5 concludes the thesis.

Chapter 2

Mathematical Model of the VSC

The objective of this chapter is to present the underlying VSC model that is used throughout this work. After giving a brief overall introduction of the control structure, the rest of the chapter focuses on each control block in detail by deriving its mathematical model. In particular, power, voltage and current control, grid synchronization and pulse with modulation will be discussed. Besides examining the control elements, four distinct operation modes of the VSC will be introduced. Once the non-linear system model is established, it will be linearized in order to perform a small-signal analysis in the next chapter.

2.1 Control System Overview

An overview of the implemented converter control scheme is presented in Fig. 2.1, where a VSC is connected to a constant active power load or a grid through a Low-Pass Filter (LPF) and a transformer. The outer control loop consists of active and reactive power controllers, which provide the output voltage angle and magnitude reference by adjusting the predefined setpoints according to a measured power imbalance. The reference voltage signal is sent to the inner control loop, consisting of cascaded voltage and current controllers, that operate in a Synchronously-rotating Reference Frame (SRF). In order to detect the system frequency at the Point of Common Coupling (PCC), for synchronization a Phase-Locked Loop (PLL) unit is included in the model. For the purposes of mathematical description, an ideal average model of the Pulse Width Modulation (PWM) unit is assumed and switching is neglected. Moreover, the DC-side is assumed not to constrain the system and thus the energy source and storage on the DC-side are considered to be sufficient.

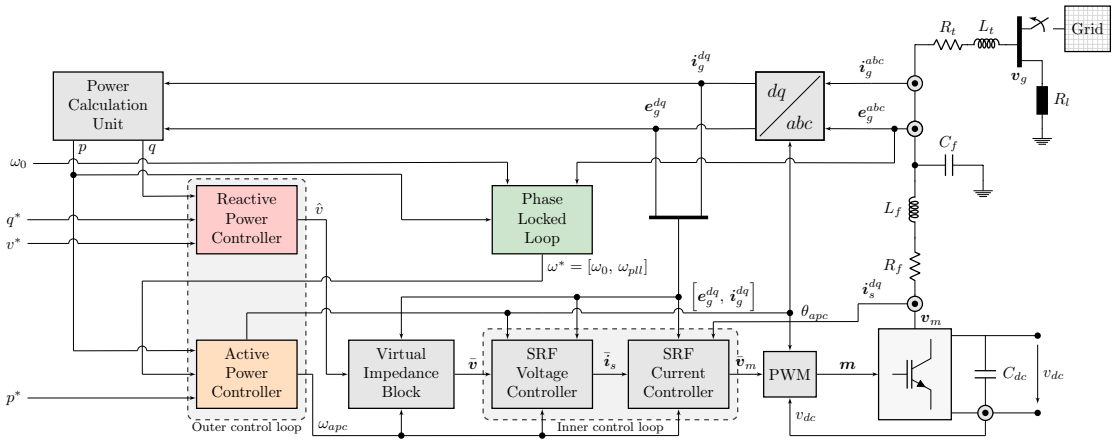

Figure 2.1: Overview of investigated and implemented VSC-control structure.

2.2 Modelling Conventions

The complete description of the converter is based on per unit quantities, denoted by lower case letters. The upper case letters in Fig. 2.1 represent physical values of the electric system. The entire modeling, analysis and control of the converter is implemented in an SRF, with the (abc/dq)-block designating a sequence of power-invariant Clarke and Park transformations from a stationary (abc)-frame to the SRF. Quantities in the SRF are written in complex space vectors such as:

$$\boldsymbol{x} = x^d + jx^q \tag{2.1}$$

with the (dq) superscript omitted in the remainder of the report. However, stationary reference frame quantities are always marked by the (abc) superscript. Additionally, the external control setpoints, e.g. the active power reference, are marked with x^*, whereas the internally computed references are represented as $\bar{x}$. The indicated current directions in Fig. 2.1 result in positive active and reactive power quantities for an energy flow from the converter into the grid.

2.3 System Modelling

The following subsections present the non-linear mathematical model for each control block and system element in Fig. 2.1. Subsequently, the derived non-linear DAE-Model will be used to establish a linearized small-signal state-space model.

2.3.1 Electric System

The VSC can be operated in either island operation or grid connected mode, as indicated in Fig. 2.1. In both cases, the electric system includes an LPF (r_f, l_f, c_f) and a transformer equivalent (r_t, l_t) to model copper and iron losses. The grid is modeled

as Thevenin equivalent, whereas the load is assumed to draw active power only. This simple structure is chosen to achieve a basic model focusing on the dynamics of the converter rather than complex AC grid topology. The SRF state space equations for the grid-connected case in pu-quantities and the SRF-coordinates can be established as:

$$\dot{\boldsymbol{i}_s} = \frac{\omega_b}{l_f}(\boldsymbol{v}_m - \boldsymbol{e}_g) - \left(\frac{r_f}{l_f}\omega_b + j\omega_b\omega_g\right)\boldsymbol{i}_s \tag{2.2}$$

$$\dot{\boldsymbol{i}_g} = \frac{\omega_b}{l_g + l_t}(\boldsymbol{e}_g - \boldsymbol{v}_g) - \left(\frac{r_g + r_t}{l_g + l_t}\omega_b + j\omega_b\omega_g\right)\boldsymbol{i}_g \tag{2.3}$$

$$\dot{\boldsymbol{e}_g} = \frac{\omega_b}{c_f}(\boldsymbol{i}_s - \boldsymbol{i}_g) - j\omega_g\omega_b\boldsymbol{e}_g \tag{2.4}$$

where $\boldsymbol{i}_s$ is the switching current flowing through the filter inductance, $\boldsymbol{v}_m$ is the modulation voltage at the converter output, $\boldsymbol{i}_g$ is the current flowing into the grid, $\boldsymbol{e}_g$ is the voltage at the filter capacitors and $\boldsymbol{v}_g$ is the voltage of the grid equivalent. The resistance and inductance of the grid are denoted as r_g and l_g, while the grid and base frequency are represented as ω_g and ω_b, respectively. For the sake of simplicity, the electric system is modeled in the SRF defined by the Active Power Control (APC).

In case of island operation the electric system equations have to be modified. Expression 2.3 changes to:

$$\dot{\boldsymbol{i}_g} = \frac{\omega_b}{l_t}(\boldsymbol{e}_g - \boldsymbol{v}_g) - \left(\frac{r_t}{l_t}\omega_b + j\omega_b\omega_g\right)\boldsymbol{i}_g \tag{2.5}$$

while defining the active load as a function of active power consumption p_{load} and constant voltage amplitude v^*_{load} as follows:

$$\boldsymbol{v}_g = r_{load}\boldsymbol{i}_g = \frac{{v^*_{load}}^2}{p_{load}}\boldsymbol{i}_g \tag{2.6}$$

It should be noted here that for a stand-alone operation the equivalent grid frequency only depends on the following factors: the external power and frequency setpoints, the actual load connected to the converter and the active power droop gain. Consequently, the overall system frequency is solely defined by the APC output.

2.3.2 Power Calculation Unit

The power calculation block processes measurements of grid voltage $\boldsymbol{e}_g$ and grid current $\boldsymbol{i}_g$. Active and reactive power are calculated as follows:

$$p = \Re(\boldsymbol{e}_g\boldsymbol{i}'_g) \tag{2.7}$$

$$q = \Im(\boldsymbol{e}_g\boldsymbol{i}'_g) \tag{2.8}$$

where $\boldsymbol{e}_g$ is the voltage at the filter capacitor and $\boldsymbol{i}'_g$ is the complex conjugate of the grid current.

2.3.3 Active Power Control

Since the focus of this work is on converter operation on a transmission grid level, the active power control has been realized using two different approaches. On the one hand, the strong coupling of active power and frequency allows to use traditional droop control, which is the standard approach for frequency control in transmission grids nowadays. On the other hand, replicating the swing equation allows for virtual emulation of the behaviour of a synchronous machine (SM), thereby recreating the inherit advantages of SMs [10,11]. Virtual Inertia Emulation (VIE) is arising as one of the potential solutions for distribution and micro-grid applications.

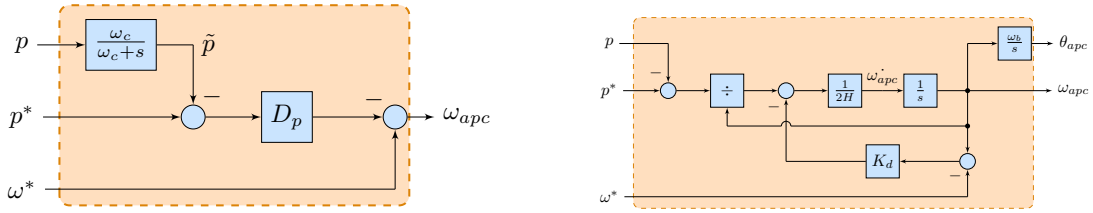

Figure 2.2: APC control schemes: (a) APC droop control block and (b) VIE control block.

For active power droop control, described by the control structure in Fig. 2.2a, the measured active power signal is passed through a first-order LPF with a cut-off frequency ω_c. Subsequently, the active power droop gain D_p regulates the output frequency ω_{apc} based on the mismatch between the filtered power measurement signal $\tilde{p}$ and the external setpoint p^*, as follows:

$$\omega_{apc} = \omega^* + D_p(p^* - \tilde{p}) \tag{2.9}$$

$$\dot{\tilde{p}} = \omega_c(p - \tilde{p}) \tag{2.10}$$

The second control scheme for virtual inertia emulation, illustrated in Fig. 2.2b, is based on a linearized conventional swing equation representing the relation between physical inertia and damping of a traditional SM. For traditional SMs the acceleration of inertia H is determined by the balance of electrical p_e, mechanical power p_m and damping power p_d:

$$\delta\dot{\omega} = \frac{1}{2H}\left(p_m - p_e - p_d\right) \tag{2.11}$$

where the mechanical and electrical power of the SM are replaced by the active power setpoint p^* and the active power output p fed into the grid. The damping term is incorporated through a feedback loop with a damping constant K_d. This feedback gain is imposed on the frequency mismatch of the APC's frequency output ω_{apc} and

an external reference ω^*. The entire block diagram showing the implementation of the swing equation is presented in Fig. 2.2b. Ergo, the virtual acceleration of normalized inertia can be formulated as:

$$\delta\dot{\omega}_{apc} = \underbrace{\frac{p^*}{2H}}_{p_m} - \underbrace{\frac{p}{2H}}_{p_e} - \underbrace{\frac{K_d}{2H}(\omega_{apc} - \omega^*)}_{p_d} \tag{2.12}$$

In steady state there is neither frequency deviation nor active power mismatch. Thus, the frequency calculated by the APC ω_{apc} is equal to grid frequency ω_g and speed deviation $\delta\omega_{apc} = \omega_{apc} - \omega_g$ vanishes. In case the converter is in island operation the APC defines the grid frequency and speed deviation is set to zero. The corresponding phase angle θ_{apc} is defined by Eqn. 2.13 and used as a reference angle for the (dq)-transformation of the entire system, thereby avoiding switching between different SRFs and simplifying the model.

$$\dot{\theta}_{apc} = \omega_{apc}\omega_b \tag{2.13}$$

2.3.4 Reactive Power Control

Analogous to the APC, the strong coupling of reactive power and voltage in transmission grid enables a droop-based implementation of reactive power control. The output voltage v is calculated as an adjustment of the external voltage setpoint v^* through reactive power droop. In order to remove the measurement noise of the calculation unit, the reactive power signal is first passed through an LPF and then compared to the reactive power setpoint q^*. The detailed control block is shown in Fig. 2.3.

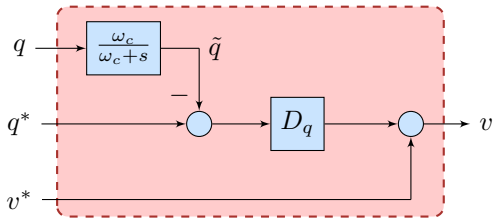

Figure 2.3: Reactive power control block.

Considering the control diagram in Fig. 2.3, the voltage reference input for the inner control loop v is defined by:

$$v = v^* + D_q(q^* - \tilde{q}) \tag{2.14}$$

where v^* and q^* are the voltage and reactive power setpoints of the VSC, respectively. D_q represents the reactive power droop gain and $\tilde{q}$ is the filtered reactive power signal. The latter is determined by the following state-equation:

$$\dot{\tilde{q}} = \omega_c(q - \tilde{q}) \tag{2.15}$$

where ω_c represents the cut-off frequency of the LPF and q is the measured reactive power.

2.3.5 Virtual Impedance

The virtual impedance concept is increasingly used for the control of power electronic systems, either embedded as an additional degree of freedom for active stabilization and disturbance rejection, or employed as a command reference generator for the converters to provide ancillary services [12]. In this thesis, virtual impedance was included in order to split the voltage amplitude reference v into (dq)-components, before passing it to the SRF voltage control. Despite maximizing active power output when set to zero, a non-zero q-component is necessary to allow for "acceleration" and "deceleration" of the virtual machine. Accordingly, minor cross-coupling of d- and q-components is needed. The virtual impedance includes a resistive r_v and an inductive element l_v. While the former is set to zero to minimize active power loss, the latter should be kept as small as feasible. The resulting d-axis and q-axis voltage components $\bar{v}^d$ and $\bar{v}^q$

$$\bar{v}^d = v - r_v i_g^d + \omega_{apc} l_v i_g^q \tag{2.16}$$

$$\bar{v}^q = -r_v i_g^q + \omega_{apc} l_v i_g^d \tag{2.17}$$

are directly used as reference for the decoupling SRF voltage controller.

2.3.6 Inner Control Loop and Modulation

The computed references for voltage, frequency and transformation angle are passed to the inner control loop as indicated in Fig 2.1. However, a direct use of such signals for Pulse-Width Modulation raises problems regarding the limitations and controlled saturation of the converter's currents and voltages [13]. These issues are conveniently resolved with a cascaded inner control scheme where the initial reference $\bar{\boldsymbol{v}}$ is processed through a sequence of voltage and current loops, yielding a more robust converter setpoint $\bar{\boldsymbol{v}}_m$. Such approach increases the flexibility of protection strategies and is commonly used in droop-controlled microgrids [7, 14].

SRF Voltage control

The structure of the SRF voltage controller follows the similar principles as the controllers in [3, 13]. The PI-controller acts on the mismatch of voltage reference $\bar{\boldsymbol{v}}$ and measurement $\boldsymbol{e}_g$ and includes the possibility to enable or disable a feed-forward of the measured current feed-forward by setting the feed-forward gain $K_{ffc} \in [0, 1]$. The reference switching current $\bar{\boldsymbol{i}}_s$ is given by:

$$\bar{\boldsymbol{i}}_s = K_{pv}(\bar{\boldsymbol{v}} - \boldsymbol{e}_g) + K_{iv}\boldsymbol{\xi} + jc_f\omega_{apc}\boldsymbol{e}_g + K_{ffc}\boldsymbol{i}_g \tag{2.18}$$

$$\dot{\boldsymbol{\xi}} = \bar{\boldsymbol{v}} - \boldsymbol{e}_g \tag{2.19}$$

where K_{pv} and K_{iv} are the proportional and the integral controller gains, respectively. The integrator state is represented by $\boldsymbol{\xi}$.

SRF Current Control

Similar to its voltage counterpart, the following SRF current controller is a conventional PI-controller with decoupling term. The modulation voltage reference $\bar{\boldsymbol{v}}_m$ is defined by:

$$\bar{\boldsymbol{v}}_m = K_{pc}(\bar{\boldsymbol{i}}_s - \boldsymbol{i}_s) + K_{ic}\boldsymbol{\gamma} + jl_f\omega_{apc}\boldsymbol{i}_s + K_{ffv}\boldsymbol{e}_g \tag{2.20}$$

$$\dot{\boldsymbol{\gamma}} = \bar{\boldsymbol{i}}_s - \boldsymbol{i}_s \tag{2.21}$$

where K_{pc} and K_{ic} are the proportional and integral current gains, $\boldsymbol{\gamma}$ is the integrator state and K_{ffv} the voltage feed-forward. The generated output voltage reference $\bar{\boldsymbol{v}}_m$ is used to determine the final modulation signal.

Pulse-Width Modulation

For the purpose of an actual implementation of the VSC switching sequence, the voltage reference signal $\bar{\boldsymbol{v}}_m$ from the current controller must be processed and converted into the modulation index $\boldsymbol{m}$. This can be achieved through means of instantaneous averaging applied to the output voltage of the converter. Furthermore, the time delay effect of PWM is neglected, which yields the following expression:

$$\boldsymbol{m} = \frac{\bar{\boldsymbol{v}}_m}{v_{DC}} \tag{2.22}$$

Neglecting any switching operation and assuming ideal PWM implementation without delays, the averaged instantaneous converter modulation voltage $\boldsymbol{v}_m$ is given by:

$$\boldsymbol{v}_m \approx \boldsymbol{m} \cdot v_{DC} \rightarrow \boldsymbol{v}_m \approx \bar{\boldsymbol{v}}_m \tag{2.23}$$

Under these assumptions the reference modulation voltage will be close to the modulation voltage itself, thereby completely decoupling the DC side from the converter model. Hence, it is not necessary to further model the DC side of the system. Nonetheless, in real operation the DC side is required to provide sufficient energy storage and might impose restrictions [3].

2.3.7 Phase Locked Loop

The PLL or synchronizing unit is implemented as a Type-2 PLL, used to estimate the grid frequency and keep the VSC synchronized to the grid [15]. The control structure is given in Fig. 2.4. The PLL uses a rather simple estimation scheme: It includes an independent, internal (dq)-transformation that transforms the stationary output voltage $\boldsymbol{e}_g^{abc}$. A PI-controller ($K_{p,pll}$, $K_{i,pll}$) is used to keep the q-component of the voltage zero.

The synchronization is achieved by aligning the d-axis of the internal SRF with the stationary (abc)-frame and diminishing the q-component, as described in [9].

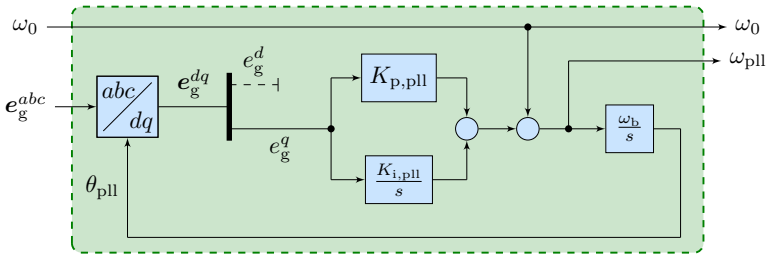

Figure 2.4: PLL control block.

The estimated frequency ω_{pll} is given by Eqn. 2.24, where ε is the integrator state. The transformation angle θ_{pll} is described by the state equation in Eqn. 2.26. It should be noted here, that the (dq)-transformation of the PLL is completely independent of the transformation used for the electrical circuit, hence adds a second SRF to the system. The alignment of these two SRFs further discussed in the next section.

$$\omega_{pll} = \omega_0 + K_{p,pll} e^q_{g,pll} + K_{i,pll}\varepsilon \tag{2.24}$$

$$\dot{\varepsilon} = e^q_{g,pll} \tag{2.25}$$

$$\dot{\theta}_{pll} = \omega_{pll}\omega_b \tag{2.26}$$

2.3.8 Aligning Reference Frames

The entire control system is implemented in the SRF defined by the APC output. When the system is in steady state the APC calculated frequency ω_{apc} equals the grid frequency, thus the corresponding angle θ_{apc} is chosen as a transformation angle to keep the system as simple as possible. All states in the presented model rotate with this frequency except the ones included in the PLL unit, since it inherits its own transformation. Consequently, the two transformations have to be properly aligned as shown in the vector diagram in Fig. 2.5.

The systems reference frame and its phase angle displacement $\delta\theta_{apc}$ are defined with respect to the voltage of a grid equivalent $\boldsymbol{v}_g$. Considering the reference amplitude of the grid voltage v_g^* the vector in the APC-oriented reference frame can be expressed as:

$$\boldsymbol{v}_g = v_g^* e^{-j\delta\theta_{apc}} \tag{2.27}$$

The PLL reference frame and its phase angle displacement $\delta\theta_{pll}$ are defined with respect to the same voltage vector. According to the definitions presented in Fig. 2.5 the angle difference between the two rotating reference frames is equal to the difference of

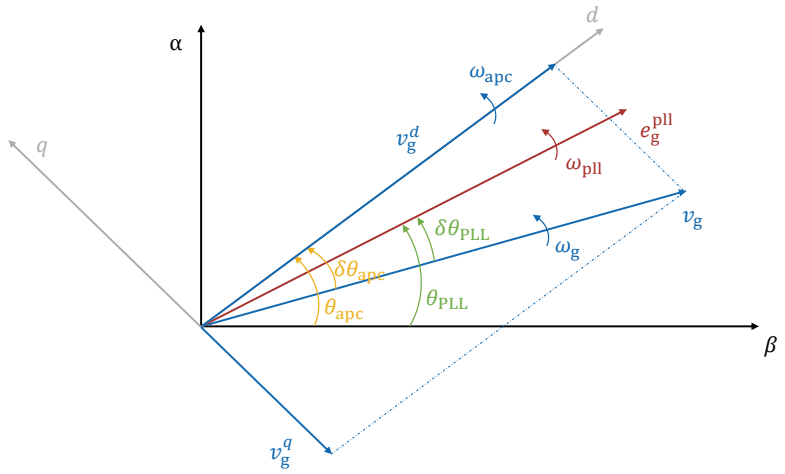

Figure 2.5: Vector diagram defining the SRF and voltage vector orientation.

the APC and PLL angles. For instance, the voltage input to the PLL can be converted from (*apc*) tp (*pll*)-reference by rotating the vector as follows:

$$\boldsymbol{e}_{g,pll} = \boldsymbol{e}_{g,apc} e^{-(\delta\theta_{pll} - \delta\theta_{apc})} \tag{2.28}$$

In section 2.3.7 the q-component of the transformed converter voltage $e^{q}_{g,pll}$ was expressed in the PLL-reference frame. In order to align it with the rest of the state equations it has to be rotated by the difference in phase angle displacements. Considering Eqn. 2.28 it follows:

$$e^{q}_{q,pll} = e^{d}_{g} \sin\left(\delta\theta_{apc} - \delta\theta_{pll}\right) + e^{g}_{g} \cos\left(\delta\theta_{pll} - \delta\theta_{apc}\right) \tag{2.29}$$

2.4 Operation Modes

The presented mathematical model offers flexibility in changing the operation mode of the VSC. Thus far, the reference inputs for the outer control loops, in particular active and reactive power, grid voltage amplitude and frequency setpoints, are externally defined, constant parameters. Indeed, the PLL-unit is not required in this operation mode, as the external frequency reference ω_0 is fed through the PLL without adjustment. Hence, a constant input is directly fed into the APC. This operation is called **grid-forming (*g*-form)**. Since there is no grid feedback required to operate the VSC, it allows for black-start and island mode applications.

Besides all outer control loop inputs being constant, the VSC can also be set up to follow the actual grid equivalent frequency. Accordingly, the PLL-unit needs to be

activated, estimates the frequency and passes the result ω_{pll} to the APC. This operation mode is called **grid-feeding(g-feed)** or **grid-following** operation, since a grid connection is required for stable operation. Consequently, the converter looses black-start possibility. The VSC can only operate when connected to frequency reference, lacking the option to supply a load in islanded operation.

The two presented cases combined with the two options for active power control lead to a total of four distinguishable operation modes to be analyzed in the consecutive chapter. An overview of the operation modes and the changes imposed on the mathematical model are given in Tab. 2.1.

Table 2.1: Overview of operation modes and the changes imposed to the mathematical model.

	Active Power Droop $\omega_{apc} = \omega^* + D_p(p^* - \tilde{p})$	**Virtual Inertia Emulation** $\delta\dot{\omega}_{apc} = \frac{1}{2H}(p^* - p) - \frac{K_d}{2H}(\omega_{apc} - \omega^*)$
g-form	PLL-Unit not active: $\omega^* = \omega_0 = 1$ p.u.	
g-feed	PLL-Unit active: $\omega^* = \omega_{pll}$	

2.5 Non-Linear System Model

All equations needed for a detailed grid-connected VSC model have been presented in the previous sections. They can be transformed into state-space notation with 15 distinct state variables and 6 inputs, where the state vector $\boldsymbol{x}$ and the input vector $\boldsymbol{u}$ are defined as:

$$\boldsymbol{x} = \begin{bmatrix} e_g^d & e_g^q & i_s^d & i_s^q & \gamma^d & \gamma^q & i_g^d & i_g^q & \dots & \\ & & \dots & \varepsilon & \xi^d & \xi^q & q_m & \delta\theta_{apc} & \delta\theta_{pll} & \begin{Bmatrix} \delta\omega_{apc} \\ \tilde{p} \end{Bmatrix} \end{bmatrix}^T \tag{2.30}$$

$$\boldsymbol{u} = \begin{bmatrix} p^* & q^* & v^* & v_g^* & \omega_0 & \omega_g \end{bmatrix}^T$$

As indicated in Eqn. 2.30 one state is changing corresponding to the activated APC. When APC droop is effective the filtered active power $\tilde{p}$ is a state, whereas speed deviation $\delta\omega_{apc}$ is a state variable for the VIE case. Besides the direct setpoints for the VSC outer control loops (p^*, q^*, v^*, ω_0), the grid equivalent voltage amplitude v_g^* and its frequency ω_g are included in the input vector.

Depending on the operation mode of the system not only the state variables, but also the state equations adapt. Eqn. 2.31 exemplary presents the state equations for **VIE** *g*-**form** in **grid-connected** operation. For the sake of of simplicity the mathematical formulation of the system in other operation modes is not included here. The steady state operation point of the VSC system is to be found by solving this non-linear DAE model with derivative terms set to zero.

$$
\begin{aligned}
\dot{e}_g^d &= \omega_b\omega_g e_g^q - \frac{\omega_b}{c_f} i_g^d + \frac{\omega_b}{c_f} i_s^d \\
\dot{e}_g^q &= -\omega_b\omega_g e_g^d - \frac{\omega_b}{c_f} i_g^q + \frac{\omega_b}{c_f} i_s^q \\
\dot{i}_s^d &= \omega_b\omega_g i_s^q - \frac{\omega_b}{l_f} e_g^d + \frac{K_{ic}\omega_b}{l_f}\gamma^d - \frac{K_{pc}\omega_b}{l_f} i_s^d + \frac{K_{ffv}\omega_b}{l_f} e_g^d - \frac{r_f\omega_b}{l_f} i_s^d + \frac{K_{ffc}K_{pc}\omega_b}{l_f} i_g^d - \frac{K_{pc}K_{pv}\omega_b}{l_f} e_g^d \\
&\quad + \frac{K_{pc}K_{pv}\omega_b}{l_f} v^* + \frac{K_{iv}K_{pc}\omega_b}{l_f}\xi^d - \frac{l_1\omega_b}{l_f}\omega_g i_s^q - \frac{l_1\omega_b}{l_f}\delta\omega_{apc} i_s^q - \frac{K_{pc}c_f\omega_b}{l_f}\delta\omega_{apc} e_g^q - \frac{D_q K_{pc}K_{pv}\omega_b}{l_f}\tilde{q} \\
&\quad - \frac{K_{pc}K_{pv}r_v\omega_b}{l_f} i_g^d - \frac{K_{pc}c_f\omega_b}{l_f}\omega_g e_g^q + \frac{D_q K_{pc}K_{pv}\omega_b}{l_f} q^* + \frac{K_{pc}K_{pv}l_v\omega_b}{l_f}\delta\omega_{apc} i_g^q + \frac{K_{pc}K_{pv}l_v\omega_b}{l_f}\omega_g i_g^q \\
\dot{i}_s^q &= \frac{K_{ic}\omega_b}{l_f}\gamma^q - \omega_b\omega_g i_s^d - \frac{\omega_b}{l_f} e_g^q - \frac{K_{pc}\omega_b}{l_f} i_s^q + \frac{K_{ffv}\omega_b}{l_f} e_g^q - \frac{r_f\omega_b}{l_f} i_s^q + \frac{K_{ffc}K_{pc}\omega_b}{l_f} i_g^q - \frac{K_{pc}K_{pv}\omega_b}{l_f} e_g^q \\
&\quad + \frac{K_{iv}K_{pc}\omega_b}{l_f}\xi^q + \frac{l_1\omega_b}{l_f}\omega_g i_s^d + \frac{l_1\omega_b}{l_f}\delta\omega_{apc} i_s^d + \frac{K_{pc}c1\omega_b}{l_f}\delta\omega_{apc} e_g^d - \frac{K_{pc}K_{pv}r_v\omega_b}{l_f} i_g^q + \frac{K_{pc}c_f\omega_b}{l_f}\omega_g e_g^d \\
&\quad - \frac{K_{pc}K_{pv}l_v\omega_b}{l_f}\delta\omega_{apc} i_g^d - \frac{K_{pc}K_{pv}l_v\omega_b}{l_f}\omega_g i_g^d \\
\dot{\gamma}^d &= -i_s^d + K_{pv}v^* - K_{pv}e_g^d - K_{pv}r_v i_g^d + K_{pv}l_v i_g^q\omega_g + K_{pv}l_v i_g^q\delta\omega_{apc} + K_{pv}D_q q^* - K_{pv}D_q\tilde{q} \\
&\quad + K_{ffc} i_g^d + K_{iv}\xi^d - c_f e_g^q\omega_g - c_f e_g^q\delta\omega_{apc} \\
\dot{\gamma}^q &= -i_s^q - K_{pv}e_g^q + K_{ffc} i_g^q + K_{iv}\xi^q + c_f e_g^d\omega_g + c_f e_g^d\delta\omega_{apc} + K_{pv}r_v i_g^q + K_{pv}l_v i_g^d\omega_g + K_{pv}l_v i_g^d\delta\omega_{apc} \\
\dot{i}_g^d &= \omega_b\omega_g i_g^q + \frac{\omega_b}{(l_g+l_t)} e_g^d - \frac{\omega_b}{(l_g+l_t)} v_g^* cos(\delta\theta_{apc}) - \frac{(r_g+r_t)\omega_b}{(l_g+l_t)} i_g^d \\
\dot{i}_g^q &= -\omega_b\omega_g i_g^d + \frac{\omega_b}{(l_g+l_t)} e_g^q + \frac{\omega_b}{(l_g+l_t)} v_g^* sin(\delta\theta_{apc}) - \frac{(r_g+r_t)\omega_b}{(l_g+l_t)} i_g^q \\
\dot{\varepsilon} &= -sin(\delta\theta_{pll} - \delta\theta_{apc}) e_g^d + cos(\delta\theta_{pll} - \delta\theta_{apc}) e_g^q \\
\dot{\xi}^d &= e_g^d - v^* + D_q(\tilde{q} - q^*) + r_v i_g^d - l_v i_g^q(\delta\omega_{apc} + \omega_g) \\
\dot{\xi}^q &= -e_g^q - r_v i_g^q - l_v i_g^d\omega_g - l_v i_g^d\delta\omega_{apc} \\
\dot{\tilde{q}} &= \omega_c\tilde{q} - \omega_c(i_g^d e_g^q - i_g^q e_g^d) \\
\delta\dot{\theta}_{apc} &= \omega_b\delta\omega_{apc} \\
\delta\dot{\theta}_{pll} &= \omega_b\omega_0 - \omega_b\omega_g + \omega_b K_{p,pll} cos(\delta\theta_{pll} - \delta\theta_{apc}) e_g^q - \omega_b K_{p,pll} sin(\delta\theta_{pll} - \delta\theta_{apc}) e_g^d + \omega_b K_{i,pll}\varepsilon \\
\delta\dot{\omega}_{apc} &= \frac{1}{2H}\left(i_g^d e_g^d + i_g^q e_g^q\right) + \frac{1}{2H}\left(K_d(\delta\omega_{apc} - \omega_0 + \omega_g)\right)
\end{aligned}
\tag{2.31}
$$

2.6 Linear Small-Signal Model

In order to perform a stability analysis of the presented VSC-model with stability assessment techniques based on eigenvalues, the state equations have to be linearized to

obtain the small-signal state-space form:

$$\Delta\dot{\boldsymbol{x}} = \boldsymbol{A}\Delta\boldsymbol{x} + \boldsymbol{B}\Delta\boldsymbol{u} \tag{2.32}$$

where a prefix Δ denotes the small deviations of the system states around the steady-state operating point $\boldsymbol{x}_0$. The resulting algebraic state-space matrices for the case presented in Eqn. 2.31 (**VIE-control, g-form**) are exemplary showcased at this point. Initial operation conditions of the states are denoted by subscript 0 in the matrix elements. The matrices follow the scheme:

$$\begin{pmatrix} \boldsymbol{\Delta}\dot{\boldsymbol{x}}_1 \\ \boldsymbol{\Delta}\dot{\boldsymbol{x}}_2 \end{pmatrix} = \begin{pmatrix} \boldsymbol{A}_{11} & \boldsymbol{A}_{12} \\ \boldsymbol{A}_{21} & \boldsymbol{A}_{22} \end{pmatrix} \begin{pmatrix} \boldsymbol{\Delta}\boldsymbol{x}_1 \\ \boldsymbol{\Delta}\boldsymbol{x}_2 \end{pmatrix} + \boldsymbol{B}\boldsymbol{\Delta}\boldsymbol{u} \tag{2.33}$$

$$\boldsymbol{A_{11}} = \begin{bmatrix} 0 & \omega_b\omega_{g0} & \frac{\omega_b}{c_f} & 0 & 0 & 0 & \frac{-\omega_b}{c_f} \\ -\omega_b\omega_{g0} & 0 & 0 & \frac{\omega_b}{c_f} & 0 & 0 & 0 \\ \frac{\omega_b\left(K_{ffv}-K_{pc}K_{pv}-1\right)}{l_f} & \frac{-K_{pc}c_f\omega_b\bar{\omega}}{l_f} & \frac{-\omega_b\left(r_f+K_{pc}\right)}{l_f} & \omega_b\left(\omega_{g0}-\bar{\omega}\right) & \frac{K_{ic}\omega_b}{l_f} & 0 & \frac{K_{pc}\omega_b\left(K_{ffi}-Kpvr_v\right)}{l_f} \\ \frac{K_{pc}c_f\omega_b\bar{\omega}}{l_f} & \frac{\omega_b\left(K_{ffv}-K_{pc}K_{pv}-1\right)}{l_f} & \omega_b\left(\bar{\omega}-\omega_{g0}\right) & \frac{\omega_b\left(-r_f-K_{pc}\right)}{l_f} & 0 & \frac{-K_{ic}\omega_b}{l_f} & \frac{-K_{pc}K_{pv}l_v\omega_b\bar{\omega}}{l_f} \\ -K_{pv} & -c_f\bar{\omega} & -1 & 0 & 0 & 0 & K_{ffi}-K_{pv}r_v \\ c_f\bar{\omega} & -K_{pv} & 0 & -1 & 0 & 0 & -K_{pv}l_v\bar{\omega} \\ \frac{\omega_b}{l_g+l_t} & 0 & 0 & 0 & 0 & 0 & \frac{-\omega_b(r_g+r_t)}{l_g+l_t} \\ 0 & \frac{\omega_b}{l_g+l_t} & 0 & 0 & 0 & 0 & -\omega_b\omega_{g0} \end{bmatrix}$$

$$\boldsymbol{A_{12}} = \begin{bmatrix} 0 & 0 & 0 & 0 & 0 & 0 & 0 & 0 \\ \frac{-\omega_b}{c_f} & 0 & 0 & 0 & 0 & 0 & 0 & 0 \\ \frac{K_{pc}K_{pv}l_v\omega_b\bar{\omega}}{l_f} & 0 & 0 & \frac{K_{iv}K_{pc}\omega_b}{l_f} & 0 & \frac{-D_qK_{pc}K_{pv}\omega_b}{l_f} & \frac{-\omega_b\left(i^q_{s0}l_f+K_{pc}\left(c_fe^q_{g0}-K_{pv}i^q_{g0}l_v\right)\right)}{l_f} & 0 \\ K_{pv}l_v\bar{\omega} & 0 & 0 & 0 & \frac{K_{iv}K_{pc}\omega_b}{l_f} & 0 & \frac{\omega_b\left(i^d_{s0}l_f+K_{pc}\left(c_fe^d_{g0}-K_{pv}i^d_{g0}l_v\right)\right)}{l_f} & 0 \\ K_{ffi}-K_{pc}r_v & 0 & 0 & K_{iv} & 0 & -D_qK_{pv} & K_{pv}i^q_{g0}l_v-c_fe^0_{g0} & 0 \\ \omega_b\omega_{g0} & 0 & 0 & 0 & K_{iv} & 0 & c_fe^d_{g0}-K_{pv}i^q_{g0}l_v & 0 \\ -\frac{\omega_b(r_g+r_t)}{l_g+l_t} & 0 & \frac{v^*_{g0}\omega_b\sin(\delta\theta_{apc0})}{l_g+l_t} & 0 & 0 & 0 & 0 & 0 \\ 0 & 0 & \frac{v^*_{g0}\omega_b\cos(\delta\theta_{apc0})}{l_g+l_t} & 0 & 0 & 0 & 0 & 0 \end{bmatrix}$$

$$\boldsymbol{A_{21}} = \begin{bmatrix} -\sin(\Delta\theta_0) & \cos(\Delta\theta_0) & 0 & 0 & 0 & 0 & 0 \\ 0 & 0 & 0 & 0 & 0 & 0 & 0 \\ -1 & 0 & 0 & 0 & 0 & 0 & -r_v \\ 0 & -1 & 0 & 0 & 0 & 0 & -l_v\bar{\omega} \\ -i^q_{g0}\omega_f & i^d_{g0}\omega_f & 0 & 0 & 0 & 0 & e^q_{g0}\omega_f \\ -\frac{i^d_{g0}}{2H} & -\frac{i^q_{g0}}{2H} & 0 & 0 & 0 & 0 & -\frac{e^d_{g0}}{2H} \\ -K_{p,pll}\omega_b\sin(\Delta\theta_0) & -K_{p,pll}\omega_b\cos(\Delta\theta_0) & 0 & 0 & 0 & 0 & 0 \end{bmatrix}$$

$$\boldsymbol{A_{22}} = \begin{bmatrix} 0 & 0 & e^d_{g0}\cos(\Delta\theta_0)+e^q_{g0}\sin(\Delta\theta_0) & 0 & 0 & 0 & 0 & -e^d_{g0}\cos(\Delta\theta_0)-e^q_{g0}\sin(\Delta\theta_0) \\ 0 & 0 & 0 & 0 & 0 & 0 & \omega_b & 0 \\ l_v\bar{\omega} & 0 & 0 & 0 & 0 & -D_q & i^q_{g0}l_v & 0 \\ -r_v & 0 & 0 & 0 & 0 & 0 & i^d_{g0}l_v & 0 \\ -e^d_{g0}\omega_f & 0 & 0 & 0 & 0 & -\omega_f & 0 & 0 \\ -\frac{e^q_{g0}}{2H} & 0 & 0 & 0 & 0 & 0 & -\frac{K_d}{2H} & 0 \\ 0 & K_{i,pll}\omega_b & K_{p,pll}\omega_b\left(e^d_{g0}\cos(\Delta\theta_0)+e^q_{g0}\sin(\Delta\theta_0)\right) & 0 & 0 & 0 & 0 & -K_{p,pll}\omega_b\left(e^d_{g0}\cos(\Delta\theta_0)+e^q_{g0}\sin(\Delta\theta_0)\right) \end{bmatrix}$$

$$\boldsymbol{B} = \begin{bmatrix} 0 & 0 & 0 & 0 & 0 & e^q_{g0}\omega_b \\ 0 & 0 & 0 & 0 & 0 & -e^d_{g0}\omega_b \\ 0 & \frac{D_q K_{pc} K_{pv} \omega_b}{l_f} & \frac{K_{pc} K_{pv} \omega_b}{l_f} & 0 & 0 & \frac{-\omega_b (K_{pc}(c_f e^q_{g0} - K_{pv} i^q_{g0} l_v))}{l_f} \\ 0 & 0 & 0 & 0 & 0 & \frac{\omega_b K_{pc}(c_f e^d_{g0} - K_{pv} i^d_{g0} l_v)}{l_f} \\ 0 & D_q K_{pv} & K_{pv} & 0 & 0 & K_{pv} i^q_{g0} l_v - c_f e^q_{g0} \\ 0 & 0 & 0 & 0 & 0 & c_f e^d_{g0} - K_{pv} i^d_{g0} l_v \\ 0 & 0 & 0 & 0 & -\frac{\omega_b \cos(\delta\theta_{apc0})}{l_g + l_t} & i^q_{g0}\omega_b \\ 0 & 0 & 0 & 0 & \frac{\omega_b \sin(\delta\theta_{apc0})}{l_g + l_t} & i^d_{g0}\omega_b \\ 0 & 0 & 0 & 0 & 0 & 0 \\ 0 & 0 & 0 & 0 & 0 & 0 \\ 0 & D_q & 1 & 0 & 0 & i^q_{g0} l_v \\ 0 & 0 & 0 & 0 & 0 & -i^d_{g0} l_v \\ 0 & 0 & 0 & 0 & 0 & 0 \\ \frac{1}{2H} & 0 & 0 & \frac{K_d}{2H} & 0 & -\frac{K_d}{2H} \\ 0 & 0 & 0 & \omega_b & 0 & -\omega_b \end{bmatrix}$$

where the following substitutions were used:

$$\Delta\theta_0 = \delta\theta_{pll0} - \delta\theta_{apc0}$$
$$\bar{\omega} = \delta\omega_{apc0} + \omega_{g0}$$

Chapter 3

Model Implementation and Verification

This chapter focuses on the model implementation and verification. First, the implementation of the non-linear DAE-model and the linearized small-signal model in MATLAB is briefly explained. Then, after introducing the model parameters, the two models are verified for two test cases.

3.1 Model Implementation in MATLAB

For the scope of this thesis not only the presented DAEs in Eqn. 2.31, but also the state equations for the remainder of operation modes were implemented in MATLAB, adapting the procedure in [16, 17] and applying ODE-solver *ode15s*. This particular solver is needed in order to solve a stiff system and allow for step inputs. After adjusting the initial conditions close enough to the actual operating point, the ODE-solver delivers precise results for both transient and steady-state operation. Simulation results are discussed and presented in the model verification in chapter 3.3. Whenever results of the non-linear mathematical model are presented in the proceeding sections, they will be marked as *DAE*.

The linearized state-space model and its matrices are derived directly on run-time in MATLAB. Therefore, the procedure presented in [18] is adapted. The same state equations as for the DAE-model are used to first calculate the symbolic systems' Jacobian matrix. In a second step all parameters and steady state operation point $(\boldsymbol{x}_0, \boldsymbol{u}_0)$ are being replaced by their numerical values in order to calculate the numerical elements of the state-space matrices. The operation point itself is determined by using the non-linear DAE-Model. Whenever results of the linearized small-signal model are shown in the subsequent sections, they will be marked as *SSM*.

3.2 Model Parameters

The operation and control parameters used for all following simulations are presented in Tab. 3.1.

Table 3.1: VSC model parameters.

Grid Parameters		**Transformer Parameters**	
grid inductance	$l_g = 0.05$ p.u.	transformer inductance	$l_t = 0.15$ p.u.
grid resistance	$r_g = 0.005$ p.u.	transformer resistance	$r_t = 0.005$ p.u.
base frequency	$\omega_b = 314.16 \frac{1}{\mathrm{s}}$		
Filter Parameters		**Outer Control Loops**	
filter inductance	$l_f = 0.08$ p.u.	active power droop	$D_p = 2\%$
filter capacitance	$c_f = 0.074$ p.u.	reactive power droop	$D_q = 0.1\%$
filter resistance	$r_f = 0.003$ p.u.	inertia constant	$H = 79.58$ ms
		damping constant	$K_d = 50$ p.u.
		cut-off frequency	$\omega_f = 0.1\omega_b$
Inner Control Loops		**PLL-Unit**	
current control proportional gain	$K_{pc} = 1.27$	PLL proportional gain	$K_{p,pll} = 0.4$
current control integral gain	$K_{ic} = 14.3$	PLL integral gain	$K_{i,pll} = 4.69$
current control feed-forward	$K_{ffc} = 0$	**Setpoints**	
voltage control proportional gain	$K_{pv} = 0.59$	active power	$p^* = 0.5$ p.u.
voltage control integral gain	$K_{iv} = 736$	reactive power	$q^* = 0$
voltage control feed-forward	$K_{ffv} = 1$	grid voltage amplitude	$v_g^* = 1.0$ p.u.
virtual resistance	$r_v = 0$	VSC-voltage	$v^* = 1.0$ p.u.
virtual inductance	$l_v = 0.2$ p.u	VSC-frequency	$\omega_0 = 1.0$ p.u.

It should be noted here, that the outer control loop parameters for active power droop and virtual inertia emulation have chosen to be equivalent. The equivalence of these two active power control options was introduced in [19]. Hence, the parameters for VIE-control are described by Eqn. 3.1. These relations are used for all coming simulations in order to make the two APC options comparable.

$$H = \frac{1}{2D_p\omega_f} \quad , \quad K_d = \frac{1}{D_p} \tag{3.1}$$

3.3 Model Verification

In order to validate the proposed control structure, a non-linear model was developed in MATLAB Simulink, with the use of a Simscape Power Systems library for the electrical system design. Subsequently, the response to a 10% step change in power setpoint was compared against the full DAE and small-signal models. The overall SSM validity has been verified for the full operating range of the VSC by multiple simulations in different

operation modes. The consecutive subsections present the simulation results for two selected operation modes.

3.3.1 Test Case I: Active Power Droop Control in Grid-Forming Operation

In this test case a step change in power setpoint of 0.1 p.u. at $t = 1$ s was simulated with the g-**form APC** converter model and the parameters given in Tab. 3.1. The plots in Fig. 3.1 present the simulation results for grid voltage and current amplitudes, their dq-composition and active, reactive power and frequency.

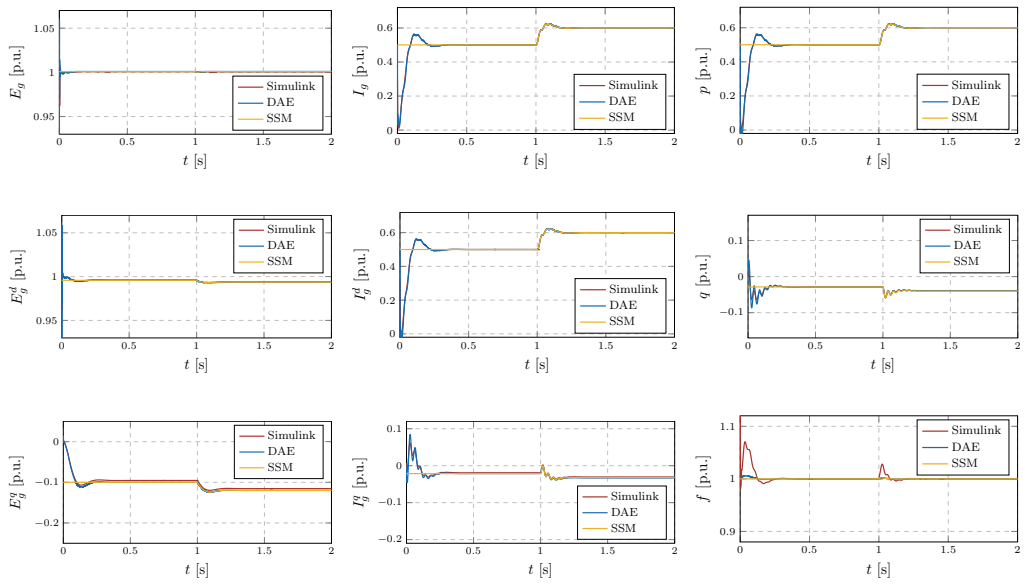

Figure 3.1: Comparing the Simulink, DAE and SSM simulation results in the case of APC droop implementation for g-form converters.

Obviously, the initialization of the Simulink and DAE-model take up to 0.3 s, even though most states initially obtain the correct steady state value. Nonetheless, the dynamic behaviour during the initialization period of those two models is identical for all states except frequency. The SSM does not show any initializing disturbances, as the operation point is directly fed to the system by the DAE simulation output.

Of more importance for system validity is the reference step change in active power at $t = 1$ s. Repeatedly, the transients occurring for all states except frequency are identical. While no discrepancies exist when comparing the non-linear DAE-model to the SSM, minor differences are observable when comparing the SSM to the Simulink model. The latter is most visible for the q-component of the converter output voltage e_g^q. Considering these scale of the plot, these differences are negligible.

The inconsistency for frequency dynamics result from the use of Simulink control blocks. These are sensitive to changes in frequency, hence result in larger overshoots. Since DAE and SSM still deliver consistent outcomes, the frequency mismatch of the Simulink model is considered not to contradict the SSM accuracy.

3.3.2 Test Case II: Virtual Inertia Emulation in Grid-Feeding Operation

In this second test case a step change in power setpoint of 0.1 p.u. at $t = 1$ s was simulated with the ***g*-feed VIE** converter model and the parameters given in Tab. 3.1. The plots in Fig. 3.2 present the corresponding simulation results.

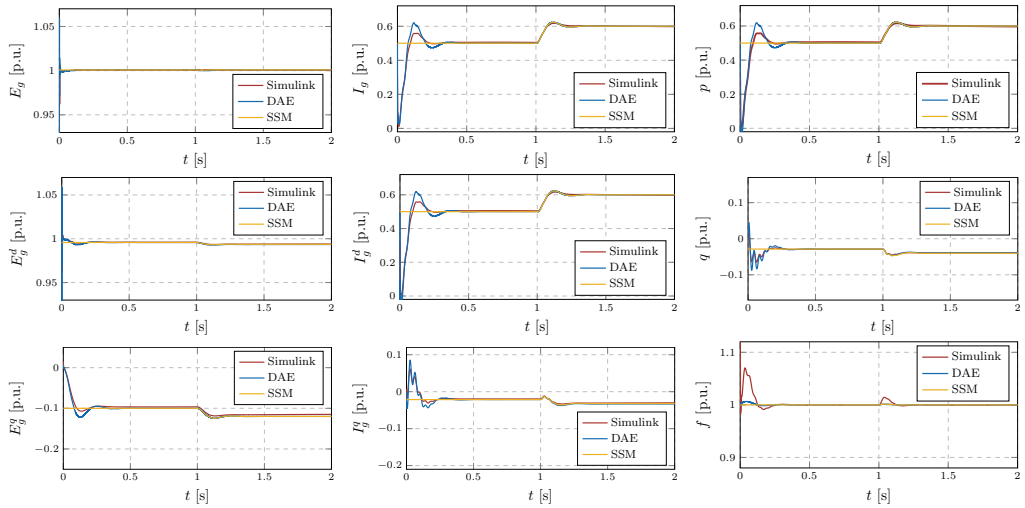

Figure 3.2: Comparing the Simulink, DAE and SSM simulation results in the case of VIE implementation for *g*-feed converters.

Similar to the first test case, only frequency seems to contradict the SSM validity, because of the Simulink model showing larger overshoots. This can, again, be explained by the use of the pre-defined control blocks in Simulink. Since all other states do not deviate for any model, both the DAE and SSM are proven to be valid.

Chapter 4

Stability Analysis

In this Chapter, the feasibility of the proposed linearized VSC converter model for the different operation modes is investigated. After analyzing the eigenvalues at the initial operating point, both APC control schemes are further studied by performing several parameter sweeps. Furthermore, the RPC parameters are tuned and the impact of PLL parameters is examined. Finally, the effect of the grid equivalent on overall converter stability in combination with the different APC control and frequency control schemes is analyzed.

4.1 Eigenvalues at Operation Point

A typical method to asses the stability of a state-space system is to analyze the eigenvalues of its state-space matrix $\boldsymbol{A}$. In order for a system to be stable, all eigenvalues have to be located on the left half-plane (LHP) of the complex plane, meaning:

$$\Re(\lambda) \leq 0 \tag{4.1}$$

where λ is the complex pole of the system. While a pole on the imaginary axis causes an oscillating term, a pole on the LHP introduces an exponentially decaying component to the system response. The rate of decay is determined by the location of the pole: those far apart from the origin result in a rapid decay.

The plot in Fig. 4.1 and Tab. 4.1 contain all 15 eigenvalues for the operation conditions given in Tab. 3.1 for the four distinct converter modes. First of all, the eigenvalues in g-form operation of the converter are independent of APC configuration. Due to the PLL unit not being active and the absence of a frequency feedback-loop in g-form operation, the different processing of the input signal does not influence the location of the poles. On the other hand, the location of poles differs for g-feed operation. The PLL-unit is active in this case and the different processes of establishing frequency setpoints for the inner control loops leads different pole locations. While in the case of APC droop control power mismatch is used to calculate the frequency setpoint, VIE directly processes frequency deviation. In the latter case, inertia imposes damping to

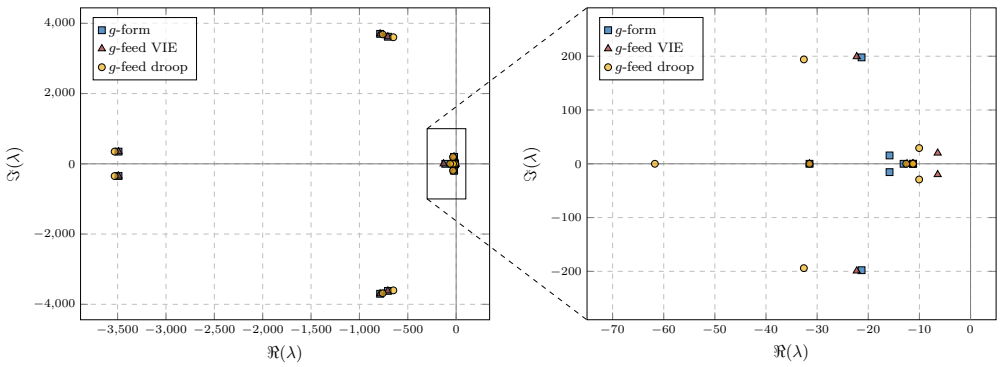

Figure 4.1: Location of eigenvalues on imaginary plane for the given point of operation and different control options.

Grid-Forming	**Grid-Following**	
Droop & Virtual Inertia	Droop Control	Virtual Inertia
$\lambda_{1,2} = -11.26$	$\lambda_{1,2} = -11.26$	$\lambda_{1,2} = -11.26$
$\lambda_3 = -13.09$	$\lambda_3 = -12.58$	$\lambda_3 = -12.42$
$\lambda_4 = -31.49$	$\lambda_4 = -31.49$	$\lambda_4 = -31.49$
$\lambda_5 = -112.25$	$\lambda_5 = -61.74$	$\lambda_5 = -129.83$
$\lambda_{6,7} = -15.84 \pm j15.52$	$\lambda_{6,7} = -10.51 \pm j29.21$	$\lambda_{6,7} = -6.43 \pm j20.02$
$\lambda_{8,9} = -21.31 \pm j197.88$	$\lambda_{8,9} = -32.59 \pm j194.04$	$\lambda_{8,9} = -22.26 \pm j199.23$
$\lambda_{10,11} = -705.55 \pm j3618.1$	$\lambda_{10,11} = -649.44 \pm j3602.8$	$\lambda_{10,11} = -705.75 \pm j3617.8$
$\lambda_{12,13} = -785.86 \pm j3699.9$	$\lambda_{12,13} = -759.37 \pm j3684.4$	$\lambda_{12,13} = -786.06 \pm j3699.6$
$\lambda_{14,15} = -3490.6 \pm j347.4$	$\lambda_{14,15} = -3530.6 \pm j348.24$	$\lambda_{14,15} = -3490.2 \pm j347.3$

Table 4.1: Eigenvalues at operation point

the system and results in poles being the closest to the imaginary axis. Hence, VIE control operation with equivalent APC droop control parameters responds slowest, but mostly damped.

For each operation mode there exist several eigenvalues close to the origin, that cause

poor damping. Furthermore, there are two complex-conjugate pole pairs per operation with poor damping and high oscillation frequency (λ_{10} to λ_{13}). Three poles on the real axis, that are marked in red in Tab. 4.1, are not effected by changing converter operation.

To conclude, the system is stable for any of the four investigated operation modes at the given operating point. The critical eigenvalue λ^*, meaning the eigenvalue closest to the imaginary axis, is largest for VIE control in g-feed mode, while g-form operation imposes the largest stability margin. The subsequent section analyzes the stability margins for changing various control parameters.

4.2 Tuning the Power Control Loops

The impact of outer control gain parameters has been investigated by alternating reactive power droop control gain in combination with either APC droop gain or inertia constant and damping. The subsequent sections present resulting stability maps and surfaces, as well as their margins.

4.2.1 Active Power Droop

When varying active power droop parameters (LPF cutoff frequency ω_c and droop gain D_p), the simulations show no effect of filter cutoff frequency on the critical eigenvalue. Hence, for APC droop control only droop gains impose restrictions. The stability map depicted in Fig. 4.2 indicates that for traditional active power droops in the range of $D_p \in [1\%, 5\%]$ all investigated VSC operation modes obtain stability. However, only g-form operation allows to meet potentially faster power response requirements and preserves a stability margin for $D_p > 10\%$. Furthermore, common reactive power droop gains around $D_q = 2\%$ do not effect stability.

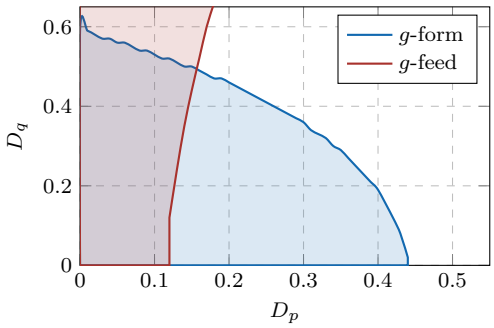

Figure 4.2: Stability map of different converter modes on the D_p-D_q plane. The system is stable in the shaded region.

The stability margin, particularly the distance of the critical eigenvalue to the imaginary axis, is illustrated in Fig. 4.3. Any set of droop gains (D_p, D_q) located above the green zero surface is stable. These surface plots indicate that no matter the VSC mode,

the critical eigenvalue stays close to the imaginary axis. While for g-form operation it saturates for $D_p < 40\%$, there exists a clear optimum for g-feed VSC mode. The maximum stability margin in the latter case can be established with active droop gain $D_p = 2.5\%$. Repeatedly, the surfaces presented in Fig. 4.3 emphasize there is no influence of reactive droop on either stability or stability margins in the range of traditional parameterization.

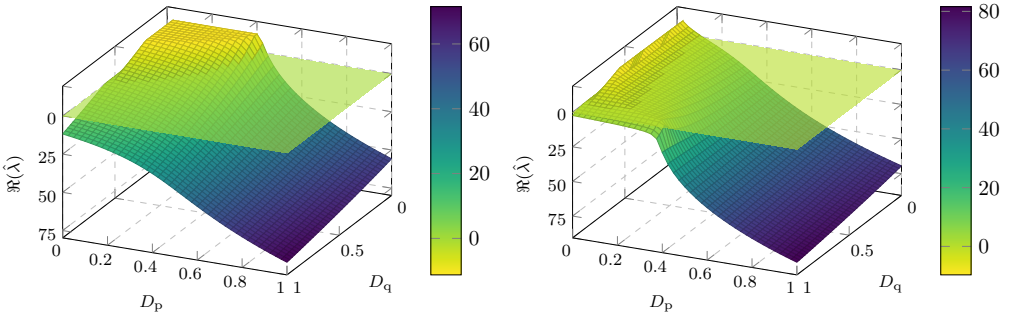

Figure 4.3: Critical eigenvalue $\hat{\lambda}$ for (a) g-form and (b) g-feed VSC operation of APC droop control.

To conclude, in active power droop control g-form VSCs allow for increased operational flexibility in tuning the outer control parameters, in general impose larger stability margins and preserve stability for high responsive converters. However, stability margins for both VSC modes can be matched by optimizing the active power droop gain for g-feed operation.

4.2.2 Virtual Inertia Emulation

When alternating VIE control parameters active power control variables, inertia and damping constants, significantly effect the movement of the critical eigenvalue. Hence, before analyzing active and reactive control parameters altogether, the first stability assessment investigates the requirement of inertia for stable operation.

Fig. 4.4 illustrates the movement of the critical eigenvalue on the complex plane for different inertia constants and converter operation, while damping is fixed to $K_d = 1$ p.u. As system inertia decreases below 50 ms, the critical pole pair steadily moves to the right hand side, resulting in minimum required inertia of $H^* = 40.6$ ms and $H^* = 46.5$ ms for g-form and g-feed operation, respectively. Again, g-form controllers obtain a higher stability margin, e.g. lower inertia requirements.

Nonetheless, this observation is only valid for damping below $K_d < 1.85$ p.u., as the stability map included in Fig. 4.5 suggests. For reasonable damping gain of $K_d = 10$ p.u., that is equivalent to $D_p = 1\%$, grid-feeding operation requires less inertia than grid-

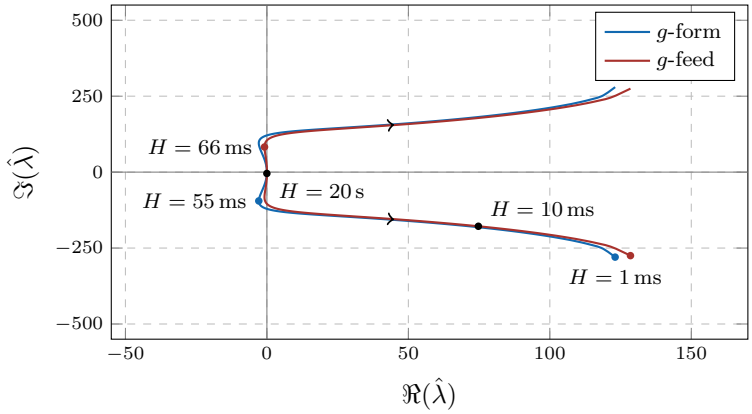

Figure 4.4: Movement of the critical eigenvalue $\hat{\lambda}$ with changing inertia for different operation modes and $K_d = 1$ p.u.

forming converters. As soon as damping exceeds $K_d > 18$ p.u. the demand of inertia rapidly decreases and basically no inertia is needed to preserve the converter stable.

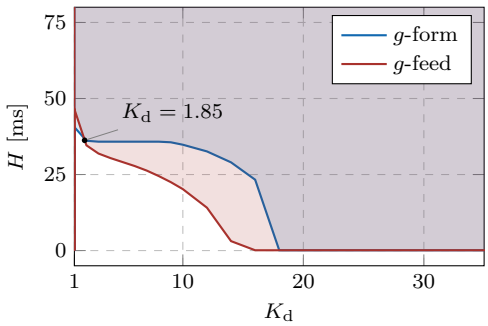

Figure 4.5: Stability map of different converter modes in the H-K_d plane. The system is stable in the shaded region.

Complementary findings are showcased in Fig. 4.6, where reactive power droop gain is additionally taken into consideration. Any operation point above the shaded surface is stable. In the investigated range of damping, grid-feeding converters need considerably less inertia than grid-forming converters, no matter the reactive droop gain. Due to the different bending, the two surfaces in Fig. 4.6a are only approaching each other for declining damping and small reactive power droops.

Examining the stability surfaces in Fig. 4.6b and Fig. 4.6c further, indicates that critical inertia H^* generally rises with increasing reactive droop gain. On the other hand, the trajectories for constant $D_p = 0.25\%$ (red line) and $D_p = 0.025\%$ (yellow line) depict, that for g-form operation and high reactive power droops the requirement for

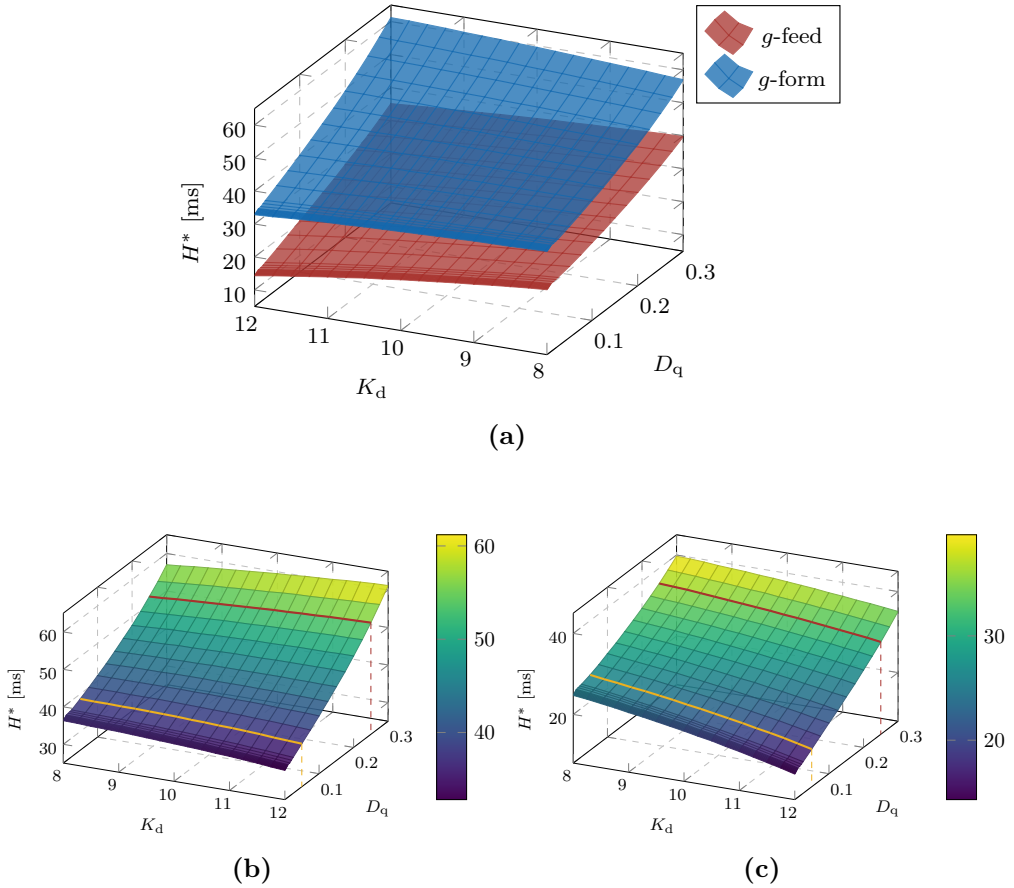

Figure 4.6: Stability surfaces for VIE control in different converter operation: inertia requirement depending on damping constants and reactive power droop gains in (a) combined plot, (b) for grid-forming and (c) grid-feeding converter mode.

inertia increases with increase in damping. Consequently, the general rule that increase in damping will reduce inertia requirements is true only for g-feed operation or g-form converters with low reactive power droops.

To sum up, the stability margins are the highest for low reactive power gains joint with high damping as this combination minimizes the inertia requirements. However, once the damping exceeds a threshold of $K_d > 20$ p.u., being equivalent to an active power droop gain of $D_p = 5\%$, no more inertia is needed for stability.

4.3 Tuning PLL Control Parameters

When operating the VSC in grid-feeding mode, the PLL unit is activated and thus influences stability and its margins. Fig. 4.7 depicts the dependence of critical inertia

on PLL control parameters exemplary for moderate damping $K_d = 10$ p.u. in order to detect the impact of the PLL parameters on stability. As shown in section 4.2.2, the inertia requirements would decrease significantly for higher damping constants.

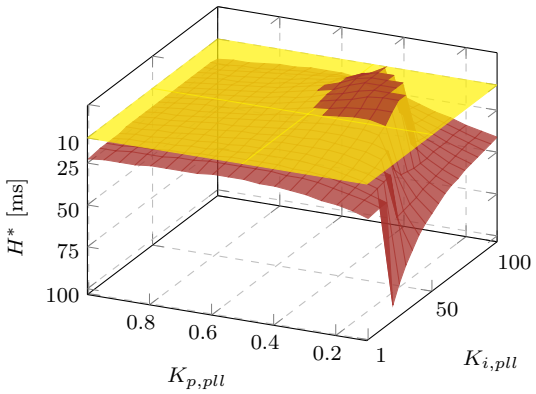

Figure 4.7: Critical inertia for varying PLL control parameters in g-feed VIE operation for damping $K_d = 10$ p.u., equivalent to active droop $D_p = 1\%$.

The yellow shaded area in Fig. 4.7 marks the range of parameter sets where inertia requirements fall below $H^* = 10$ ms. These parameter sets are located above the yellow surface in the plot. The requirement for inertia minimizes for $K_{p,pll} \in (0.3, 0.5)$ and $K_{i,pll} \in (50, 70)$. For the purpose of optimizing PLL-performance, the PLL control parameters should be chosen in this area. Indeed, poor tuning of the PLL can maximize the requirements for inertia and destabilize the system, as the clear maximum of inertia requirement $H^* = 94$ ms suggests.

Conclusively, the performed analysis indicate considerable correlation of critical inertia on PLL control parameters. If no further investigation of the VSC system is possible, proportional gain should be chosen to exceed $K_{p,pll} > 0.4$ and integral gain to exceed $K_{i,pll} > 50$ in order to increase stability margins.

4.4 Influence of the Grid Equivalent

After having analyzed the impact of the power controls themselves on overall system stability, this section will investigate the impact of the grid equivalent on VSC stability. In order to study this impact, different Short Ciruit Ratios (SCRs) will be considered. Up to here, the SCR, expressed as $\eta = x_g^{-1}$, has always been assumed to be $\eta = 20$, representing an infinite bus.

The analysis depicted in Fig. 4.8 shows the critical eigenvalue for changing SCR, incorporated in the model by changing the grid impedance accordingly, while preserving the transmission system ratio $x_g/r_g = 10$ constant. The conducted simulations indicate

no influence of the APC implementation for grid-forming operation. As long as the VSC is operated in g-form any grid, e.g. weak grids with $\eta = 0.1$, can be supplied stable. Nonetheless, for g-feed controllers VIE implementation offers more flexibility to connect weaker grids, as APC droop control can only connect systems with SCR exceeding $\eta > 1$.

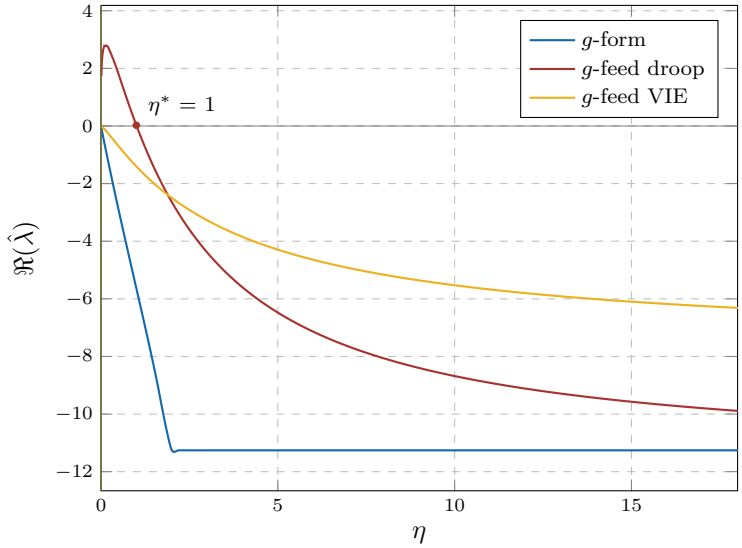

Figure 4.8: SCR influence on critical eigenvalue with initial operation parameters for different operation modes with model parameters specified in Tab. 3.1 and $x_g/r_g = 10$.

Since this analysis has been done with fixed outer control parameters as defined in Tab. 3.1, the subsequent sections will evaluate the impact of droop gains and inertia on critical SCR for g-feed operation.

4.4.1 Influence of the Grid Equivalent on APC Droop Control in g-feed Operation

The findings presented in Fig. 4.9 confirm a high contribution of active power droop gains in critical SCRs η^*. In general, the lower the active power droop gain, the weaker the grid equivalent can be. Fig. 4.9a confirms that VSCs connected to typical high-voltage systems, usually described with $\eta \approx 3$, are capable of withstanding the traditional droop control gains of up to 5%. However, a faster provision of frequency reserves would be possible only in a very stiff grid, closer to an infinite bus ($\eta > 15$).

While critical SCRs highly depend on active power droop gains, a significant influence of reactive droop gains D_q could only be detected in combination with high active power droop gains D_p, as presented in Fig. 4.10. For high responsive converters, the critical SCRs decreases with rising reactive gain.

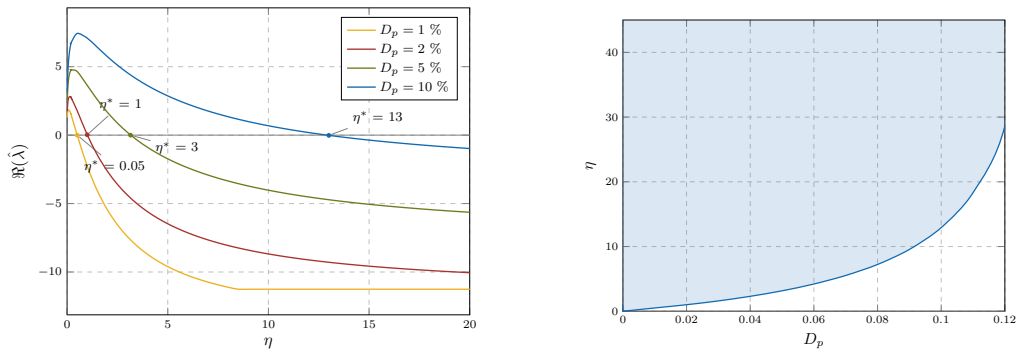

(a) **(b)**

Figure 4.9: Influence of active power droop gain and (a) SCR on critical eigenvalue and (b) resulting stability map on D_p-η plane: the shaded region is stable, with constant reactive droop $D_q = 0.01\%$.

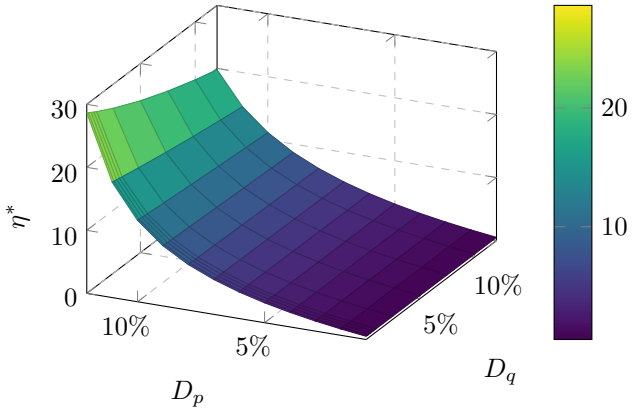

Figure 4.10: Influence of active and reactive power droop gains on critical SCR η^*: any operation point above the surface is stable.

To conclude thus far, high active power droops are only feasible for strong grids in g-feed operation. The reactive power droop gain, thereby, does not significantly influence stability and its margins. Nonetheless, when connecting VSCs to traditional grids in g-feed operation, active power droop gain needs to be chosen carefully in order to provide sufficient stability margin.

4.4.2 Influence of SCR on VIE Control in g-feed Operation

Since APC droop control was identified to be critical when combined with grid-feeding controllers and weaker grids, VIE control might be the more feasible option, as indicated in Fig. 4.8. Indeed, having a VIE controller gives significant operational flexibility, since such g-feed unit can operate even weak systems ($\eta \approx 0.1$). However, there is a mini-

mum feasible SCR. Fig. 4.11 depicts the critical eigenvalue in dependence of the SCR for equivalent active power droop gains and indicates that low inertia paired with low damping leads to the existence of critical SCRs.

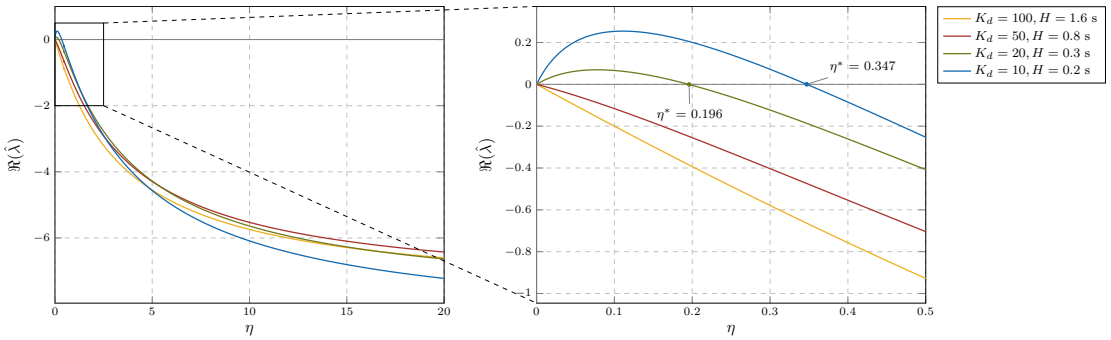

Figure 4.11: Influence of inertia emulation and SCR on critical eigenvalue; the parameters for damping and inertia correspond to the active power gains in Fig. 4.9a.

Fig. 4.12 investigates the influence of inertia and damping on critical SCRs separately, where any parameter set above the given lines is stable. It indicates that an increase in inertia stabilizes VSCs even if connected to weaker grids. Repeatedly, the higher the damping, the lower the requirement of inertia for a given SCR.

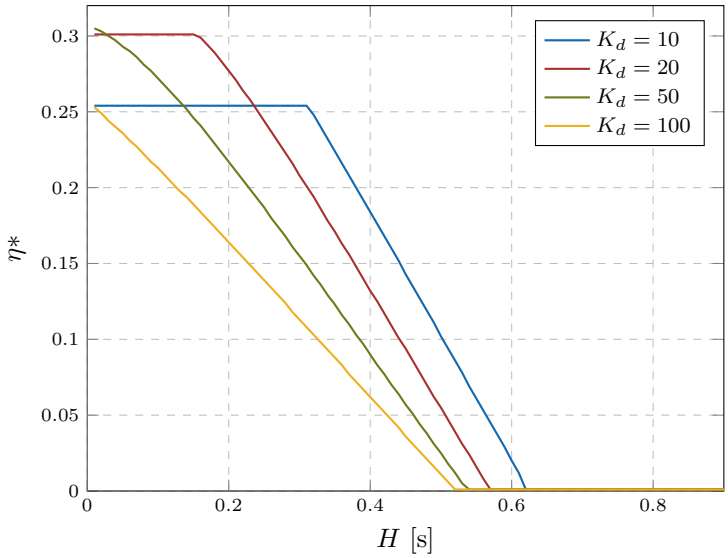

Figure 4.12: Critical SCR η^* in dependence of inertia H for different damping constants K_d.

To sum up, VIE controllers offer considerably more operational flexibility for g-feed

converters. Nonetheless, when the virtual inertia is low and the VSC is connected to a weak grid, a significant amount of damping is required to ensure stable operation and provide sufficient stability margin.

Chapter 5

Outlook and Conclusion

In this project, a detailed DAE model of a VSC was presented, including outer control, inner control and a PLL. This model was linearized in order to apply small-signal stability analysis techniques and then implemented in MATLAB. Once, the DAE and small-signal models were validated for the full range of operation, eigenvalue analysis and various bifurcation studies were conducted. Both grid-forming and grid-feeding concepts have been considered, together with different active power control configurations based on droop and VIE control.

It was shown that the stability margins of proposed operation modes can vary significantly with respect to parameter sensitivity and robustness. In general, grid-forming converters have shown larger stability margins and were identified to react less sensitive to changing parameters for both active power droop and VIE control. In the case of high-responsive converters with large active droop gains, grid-feeding converters face a lack of stability margin and might not be able to preserve stable operation. On the other hand, VIE controlled grid-forming converters were shown to require more inertia for realistic damping. However, the inertia requirements were small for both frequency configurations.

In addition, the PLL control parameters were shown to significantly influence inertia requirements and stability margins. Furthermore, the strength of the grid equivalent can impose constraints on the optimal tuning of converters, especially in case of a droop-based grid-feeding unit. VIE controllers offer considerably more operational flexibility in grid-feeding operation and retain stable even for weak grids. Nonetheless, when virtual inertia is low a significant amount of damping is required.

As all of the presented analyses were conducted for a single converter connected to a grid equivalent, future work should focus an multi-converter systems and the potential interaction between them, as well as the stability in presence of conventional synchronous machines.

Bibliography

[1] A. Ulbig, T. S. Borsche, and G. Andersson, "Impact of Low Rotational Inertia on Power System Stability and Operation," *ArXiv e-prints*, Dec. 2013.

[2] S. D'Arco, J. A. Suul, and O. B. Fosso, "Control system tuning and stability analysis of virtual synchronous machines," in *2013 IEEE Energy Conversion Congress and Exposition*, Sept 2013.

[3] S. D'Arco, J. A. Suul, and O. B. Fosso, "Small-signal modelling and parametric sensitivity of a virtual synchronous machine," in *2014 Power Systems Computation Conference*, Aug 2014.

[4] S. D'Arco, J. A. Suul, and O. B. Fosso, "A virtual synchronous machine implementation for distributed control of power converters in smartgrids," *Electric Power Systems Research*, vol. 122, pp. 180–197, 2015.

[5] N. Pogaku, M. Prodanovic, and T. C. Green, "Modeling, analysis and testing of autonomous operation of an inverter-based microgrid," *IEEE Transactions on Power Electronics*, vol. 22, pp. 613–625, March 2007.

[6] T. Green and M. Prodanović, "Control of inverter-based micro-grids," *Electric Power Systems Research*, vol. 77, no. 9, pp. 1204 – 1213, 2007.

[7] J. Rocabert, A. Luna, F. Blaabjerg, and P. Rodrguez, "Control of power converters in ac microgrids," *IEEE Trans. Power Electron.*, vol. 27, pp. 4734–4749, Nov 2012.

[8] R. Ofir, U. Markovic, P. Aristidou, and G.Hug, "Droop vs. virtual inertia: Comparison from the perspective of converter operation mode," in *2018 IEEE International Energy Conference (ENERGYCON)*, June 2018.

[9] U. Markovic, O. Stanojev, P. Aristidou, and G. Hug, "Partial grid forming concept for 100% inverter-based transmission systems," in *2018 IEEE Power and Energy Society General Meeting (PESGM)*, Aug 2018.

[10] H. P. Beck and R. Hesse, "Virtual synchronous machine," in *2007 9th International Conference on Electrical Power Quality and Utilisation*, Oct 2007.

[11] J. Driesen and K. Visscher, "Virtual synchronous generators," in *2008 IEEE Power and Energy Society General Meeting - Conversion and Delivery of Electrical Energy in the 21st Century*, July 2008.

[12] X. Wang, Y. W. Li, F. Blaabjerg, and P. C. Loh, "Virtual-impedance-based control for voltage-source and current-source converters," *IEEE Transactions on Power Electronics*, vol. 30, pp. 7019–7037, Dec 2015.

[13] S. D'Arco, J. A. Suul, and O. B. Fosso, "Virtual synchronous machines - classification of implementations and analysis of equivalence to droop controllers for microgrids," in *2013 IEEE Grenoble Conference*, June 2013.

[14] J. C. Vasquez, J. M. Guerrero, A. Luna, P. Rodriguez, and R. Teodorescu, "Adaptive droop control applied to voltage-source inverters operating in grid-connected and islanded modes," *IEEE Transactions on Industrial Electronics*, vol. 56, pp. 4088–4096, Oct 2009.

[15] S.-K. Chung, "A phase tracking system for three phase utility interface inverters," vol. 15, no. 3, pp. 431–438.

[16] "Solve differential algebraic equations (daes) - matlab & simulink - mathworks switzerland." `https://ch.mathworks.com/help/symbolic/solve-differential-algebraic-equations.html`. (Accessed on 02/22/2018).

[17] "Solve daes using mass matrix solvers - matlab & simulink - mathworks switzerland." `https://ch.mathworks.com/help/symbolic/solve-daes-using-mass-matrix-solvers.html`. (Accessed on 02/22/2018).

[18] "Linearize non-linear system using matlab/simulink." `https://ch.mathworks.com/matlabcentral/answers/56183-linearize-non-linear-system-using-matlab-simulink`. (Accessed on 02/27/2018).

[19] S. D'Arco and J. A. Suul, "Equivalence of virtual synchronous machines and frequency-droops for converter-based microgrids," *IEEE Transactions on Smart Grid*, vol. 5, no. 1, pp. 394–395, 2014.